Coupled Morphological–Hemodynamic Computational Analysis of Type B Aortic Dissection: A Longitudinal Study

Huijuan Xu [iD],[1,2] Marina Piccinelli,[3] Bradley G. Leshnower,[4] Adrien Lefieux,[2,5] W. Robert Taylor,[5,6] and Alessandro Veneziani[2,7]

[1]The George W. Woodruff School of Mechanical Engineering, Georgia Institute of Technology, Atlanta, USA; [2]Department of Mathematics and Computer Science, Emory University, Atlanta, USA; [3]Department of Radiology and Imaging Sciences, Emory University, Atlanta, USA; [4]Department of Surgery, Emory University, Atlanta, USA; [5]Department of Cardiology, Emory University, Atlanta, USA; [6]Atlanta VA Medical Center, Atlanta, USA; and [7]School of Advanced Studies IUSS, Pavia, Italy

Associate Editor Umberto Morbiducci oversaw the review of this article.

Abstract—Progressive false lumen aneurysmal degeneration in type B aortic dissection (TBAD) is a complex process with a multi-factorial etiology. Patient-specific computational fluid dynamics (CFD) simulations provide spatial and temporal hemodynamic quantities that facilitate understanding this disease progression. A longitudinal study was performed for a TBAD patient, who was diagnosed with the uncomplicated TBAD in 2006 and treated with optimal medical therapy but received surgery in 2010 due to late complication. Geometries of the aorta in 2006 and 2010 were reconstructed. With registration algorithms, we accurately quantified the evolution of the false lumen, while with CFD simulations we computed several hemodynamic indexes, including the wall shear stress (WSS), and the relative residence time (RRT). The numerical fluid model included large eddy simulation (LES) modeling for efficiently capturing the flow disturbances induced by the entry tears. In the absence of complete patient-specific data, the boundary conditions were based on a specific calibration method. Correlations between hemodynamics and the evolution field in time obtained by registration of the false lumen are discussed. Further testing of this methodology on a large cohort of patients may enable the use of CFD to predict whether patients, with originally uncomplicated TBAD, develop late complications.

ABBREVIATIONS

CFD	Computational fluid dynamics
AD	Aortic dissection
TBAD	Type B AD
uTBAD	Uncomplicated TBAD
FL	False lumen
TL	True lumen
OMT	Optimal medical therapy
WSS	Wall shear stress
TAWSS	Time averaged WSS
RRT	Relative residence time
OSI	Oscillatory shear index
3WK	3 Element windkessel model

INTRODUCTION

In aortic dissections (AD), tears occur in the intimal layer of the aortic wall, allowing blood to flow in and divide the intimal-medial layer of the arterial wall. This, in turn, creates a new channel of blood flow known as the "false lumen" (FL).[18] The original lumen is referred to as the "true lumen" (TL). AD is considered acute if the diagnosis is made within 2 weeks after onset of the symptoms, otherwise it is considered chronic.[10] AD distal to the left subclavian artery is classified as "type B". Uncomplicated TBAD (uTBAD), i.e. without malperfusion or rupture, are currently treated with optimal medical treatment (OMT). These patients have excellent short-term results; however, the long-term outcomes with OMT is poor.[1,21,29] There is a current debate regarding the optimal ther-

Address correspondence to Huijuan Xu, The George W. Woodruff School of Mechanical Engineering, Georgia Institute of Technology, Atlanta, USA. Electronic mail: hxu72@gatech.edu

apy for patients with uTBAD. Thoracic endovascular aortic repair (TEVAR) has been proposed as an alternative therapy for these patients, to prevent later aneurysm formation and improve long-term outcomes. However, the prognostic factor for using TEVAR for acute uTBAD is controversial and currently under investigation.

Ideally, anatomic risk factors could be identified based upon non-invasive imaging at the initial diagnosis of acute uTBAD to predict patients developing complications in the chronic phase. Previous investigations have identified simple anatomic criteria (e.g., maximal thoracic aortic diameter, FL expansion rate, size and location of the entry tear) that are potential risk factors for FL dilation and subsequent rupture.[9,12,20,27] However, there is a high variability in the results of these studies that limits their predictive value. Furthermore, the morphological evolution of the FL in three dimensions is complex, therefore simple measures such as diameters cannot fully represent the global changes. Collectively, these issues require advanced image-based analyses.

Moreover, identifying a set of criteria solely based on the geometry of the FL leaves an incomplete picture. For example, controversy also exists on the impact of FL thrombosis upon aneurysm formation and mortality.[2,19,20,30] The impact of hemodynamics on FL degeneration has been studied using CFD simulations. The effect of WSS related factors, the percentage of blood flow passing through the FL, the pressure difference between TL and FL, and also the RRT of flow inside of the FL have been studied.[3,5,6,26,31,34] However, when relating the hemodynamic factors with the FL evolution, these studies characterized the degeneration of the FL by single measurements such as the change of the maximum aortic diameter. Observational conclusions were drawn, generally on one patient, possibly with a follow-up.[5] A systematic aggregation of all hemodynamic factors and how they correlate to this disease progression is still missing.

To obtain reliable clinically relevant conclusions, patient-specific computational studies over a large number of patients enrolled in longitudinal clinical trials are needed. Consequently, efficient numerical solvers are required. In this work, we explore some specific tools devised for such clinical trials. Specifically, we consider a longitudinal data set involving a patient over 4 years. While this patient was not operated in 2006 due to the "non-risky" morphological features of the FL, 4 years later the surgery was necessary. An extensive morphological analysis[16] was performed to quantify the FL progression accurately in three dimensions. In addition, a CFD analysis of the patient-specific flow patterns was carried out to extract hemodynamic factors. By considering the morpholog-

ical changes of the entire FL and hemodynamic factors simultaneously, correlations were established to potentially help understanding the intertwining between hemodynamics and FL progression in this originally uTBAD.

In comparison with previous studies, this work brings novelty in three aspects:

(1) Quantification of the FL evolution is not based on a simple average measure like the FL volume, or the maximum diameter. Instead, registration methods were used to give a comprehensive quantification of the growth.

(2) The entry tear and the local morphology trigger flow acceleration and disturbances that challenge the numerical solution. Even if it is generally a non-turbulent flow, very fine mesh scales are typically required, which are unsuitable for large clinical studies. To combat this, we proceed by using a state-of-the-art Large Eddy Simulation modeling.[4]

(3) In our clinical case, patient-specific measurements to be used for the boundary conditions are missing. This is a common problem in clinical computational hemodynamics, as flow or pressure data are often not recorded with the images. We present a method that calibrates the parameters of a classical 3WK model at the outflows with flow rates derived from patient-specific morphology using the well-known Murray's Law.[35] The latter is used to calibrate the parameters of Windkessel models, so to convert morphological patient-specific data into hemodynamic ones.

MATERIALS AND METHODS

A 60 year-old female was admitted to the Emory University Hospital (EUH) with uTBAD in 2006. After 4 years under OMT, she was re-admitted and operated in 2010 because of the significant FL aneurysmal dilation. Two sets of computed tomography angiography (CTA) were obtained in 2006 and 2010, which will be referred as initial and follow-up cases respectively. The CTA images and general medical data were de-identified before being used in this study. Approval for this study was obtained from the EUH institutional review board.

CT Image Acquisition and Geometry Reconstruction

The details of the initial and follow-up CT acquisitions of the patient are reported in the Supplementary Materials. To reconstruct the geometry of the dissected

aorta, all DICOM slices were processed by the Vascular Modeling Toolkit (VMTK: www.vmtk.org). The procedure was manually supervised by one of the authors (MP) as the detection of the tears between the lumens was particularly challenging. The quality of the images allowed the detection of one entry tear and two distal tears in 2006, as well as one distal tear in 2010. The final reconstructed models covered the entire aorta from the sinotubular junction to the initial portion of the right and left common iliac arteries, including the major side branches visible in the images. The portion of the arteries included in the geometrical model was determined by the quality of the images. Considerable differences in anatomy were evident between the two acquisitions.

In the two geometries, we identify the following portions as the "boundaries" (Fig. 1):

(1) The arterial wall Γ_w, which is considered to be rigid.
(2) The inflow Γ_{in}, i.e. the portion corresponding to the entrance of the ascending aorta.
(3) The outflow Γ_{out}, one for each of the collateral aortic arteries (i.e. brachiocephalic trunk, left common carotid, left subclavian, superior mesenteric, renal arteries) and the common iliac arteries.

Quantification of the FL Evolution

In image registration,[13] one image is mapped to another with the minimization of a properly defined quantification of the mismatch. Different image registration techniques arise based on the choice of the postulated mapping and its parametrization, as well as desired constraints.

To quantify the 3D evolution of the false lumen, we adopt a point set registration (PSR) method based on a probability density estimation, to automatically co-register the initial and follow-up FL geometries.[16] This registration method transforms the so-called Gaussian mixture model centroids (representing the initial geometry) to the follow-up geometry by maximizing the likelihood. The transformation is represented by a regularized displacement field to ensure the coherent motion of the FL surface.

Comparing to the most common iterative closest point (ICP) registration methods, probability-based methods are less sensitive to the initial value and noise. Moreover, this specific variation of probability based method does not require any prior knowledge of the non-rigid transformation nor the correspondence between the two datasets.[16]

Before the non-rigid registration, a rigid registration was performed to pre-align the initial and follow-up FL, in order to filter the rigid body transformation, as shown in Fig. 2a. The proximal entry tear and superior mesenteric branch are aligned in the rigid registration. This is considered reasonable since the central line distance from the left subclavian artery to the proximal entry tear stayed the same over the years, and so is the case for the superior mesenteric artery. Then a non-rigid registration was performed between the pre-aligned FLs. The initial geometry of the FL was registered to the follow-up one, as shown in Fig. 2b (see details in Supplementary Material). Based on the non-rigid registration, a 3D deformation field, representing the evolution of FL from initial to follow-up state was computed, as shown in Fig. 2c.

Computational Fluid Dynamics

The numerical simulations are performed with the finite element solver LifeV (www.lifev.org).[22] Assumptions on blood flow and details of the simulations are specified in the Supplementary Materials.

Turbulence Modeling

The blood flow in the aorta at systolic peak is at the transitional stage to turbulence. Strong convective fields in specific geometrical configurations, like the dissected aorta, determine an energy cascade from the large scales flow structures to small scales. Consequently, in our case, we need very fine meshes to capture all the relevant scales of the dynamics of interest, in what is commonly called Direct Numerical Simulation (DNS). For large studies involving many patients, the computational costs required by DNS may be too high. Therefore, we use a state-of-art Evolve-Filter-Relax LES solver.[4] The LES solver is developed to capture the small scales in a surrogate way, with the addition of an auxiliary differential problem ("filter") to solve with the Navier–Stokes equations. LES approach is preferred to the classical Reynolds Average Navier–Stokes (RANS) approach as its more solid mathematical background allows one to better control the approximation error. Furthermore, LES also serves as a strong consistent stabilization for the numerical instabilities due to the strong convection during systole and possible backflow at distal aortic branches during diastole.

Mesh Generation

The reconstructed geometries of dissected aorta were discretized with the open source mesh generator NETGEN (http://www.hpfem.jku.at/netgen/) for finite element simulations. The mesh of the follow-up case is displayed in Fig. 1. The detailed discretization infor-
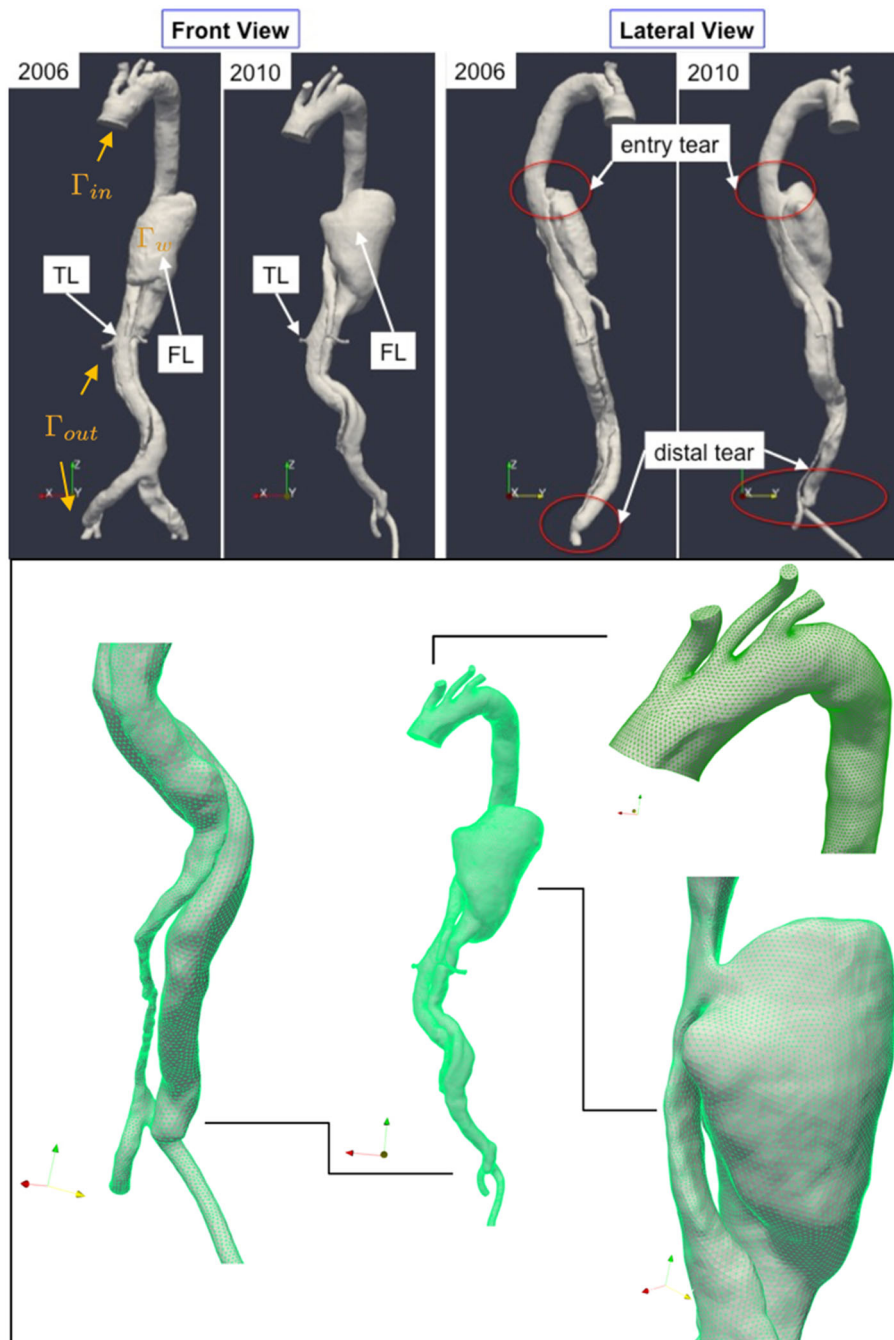
FIGURE 1. Geometry reconstruction of the dissected aorta from CT angiography. Top Left and right are front and lateral views, respectively, of the reconstructed aorta at 2006 and 2010 using VMTK. The tears of the FL are highlighted in red circles. Bottom demonstrates the mesh of the follow-up case for the numerical simulation.

mation is shown in Table 1. The mesh size must be carefully selected as a trade-off between accuracy and computational cost. The LES solver allows using relatively coarse meshes, which is a significant computational advantage in view of multi-patient studies. We tested this statement in our case. More precisely, two meshes at different refinement levels for the follow-up case were generated. The finer mesh for 2010 was used

for a direct numerical simulation, to provide a ground-truth numerical solution to be compared with the LES results. The latter is obtained with significantly less computing time (80% reduction). We verified that the LES solution on the mesh and DNS on the finest mesh are quantitatively consistent. Detailed comparisons between the results from LES and DNS for the 2010 case can be found in the Supplementary Materials.
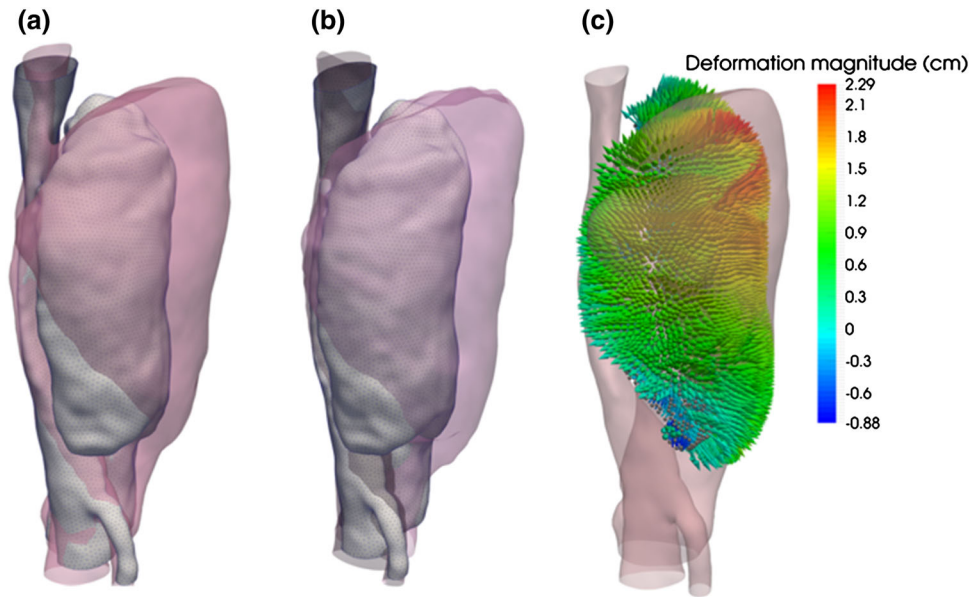
FIGURE 2. Registration of FLs. (a) Pre-aligned FLs by rigid registration. (2006: grey, 2010: pink). (b) FL at 2006 before non-rigid registration (grey) vs. FL at 2006 after non-rigid registration (pink). (c) Three-dimensional deformation field characterizing FL evolution. The deformation field was projected to the surface normal direction (outward) of the FL. The deformation vector field is colored by the deformation magnitude and is positive if the deformation vector is in the direction of the normal, negative if opposite.

TABLE 1. Parameters of the different meshes (unit: cm).

Case	#Elem	h_{min}	h_{avg}	h_{max}
Initial (2006)	934 k	1.30e−2	2.19e−2	4.04e−1
Follow-up LES (2010)	645 k	1.13e−2	3.43e−2	5.32e−1
Follow-up* DNS (2010)	1063 k	7.50e−4	2.09e−2	3.01e−1

Here, h_{min}, h_{avg} and h_{max} are the minimum, average and maximum edge length of the tetrahedra, which were computed after the meshes were generated using NETGEN.

Additionally, a mesh of the initial case was created with a level of refinement comparable to the coarse mesh of the Follow-up case.

Boundary Conditions

Results of computational hemodynamics are largely affected by both the geometry of the arteries and the boundary conditions specification.[24] Unfortunately, practical and ethical constraints still limit access to data required for a full patient-specific prescription of boundary conditions, at least in the clinical routine. The missing data are usually replaced by modeling assumptions or by adapting literature data to the case of interest. As a certain degree of arbitrariness is unavoidable, a mathematically sound approach in the selection of what data to prescribe and how is critical to reducing the impact of those non-patient specific assumptions on the final result. The selection of a strategy must be reliable and computationally efficient.

Specifically, the rigid assumption promptly leads to the null-velocity condition

$$\boldsymbol{u}(\Gamma_w, t) = 0, \forall t > 0.$$

For Γ_{in}, we adopted the flow rate Q_{in} from previous study, as shown in Fig. 3.[7] With the given flow rate, a flat velocity profile was enforced accordingly at the inlet.

For the outflow sections Γ_{out}, it is more difficult to adopt literature data, due to the variation of the morphology and of the quality of the reconstruction. Therefore, we decided to resort to a specific surrogate modeling strategy. As the only available patient specific data is the geometry, we elaborate a novel method that efficiently converts morphological information on the patient into boundary data to prescribe. The Murray's law, defining the flow rate entering an outflow branch based on the vessel diameter, and the inlet diameter Q_{in} reads
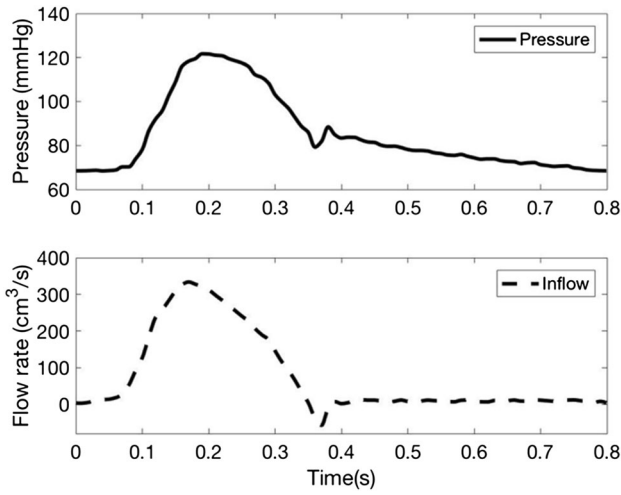
FIGURE 3. Waveform for pressure and velocity used at the inflow as well as for the calibration of the 3WK parameters.

$$\frac{Q_b}{Q_{in}} = \left(\frac{d_b}{d_{in}}\right)^s,$$

where s is an empirical parameter in the range [2, 3] and d_b and d_{in} are the diameters of the branch and the inflow. For non-circular sections the diameter defined as the hydraulic diameter

$$d_b = 2\sqrt{\left(\frac{A_b}{\pi}\right)}, \ d_{in} = 2\sqrt{\left(\frac{A_{in}}{\pi}\right)}.$$

This condition could be converted into a velocity condition by postulating a velocity profile fit to the given flow rate. A delicate aspect is that, in general, Murray's Law does not guarantee the condition

$$Q_{in}(t) = \sum_b Q_b(t),$$

required in a rigid domain by the mass conservation principle. A typical workaround could be to prescribe traction free conditions on one of the outflow sections,

$$-p\boldsymbol{n} + \mu\left(\nabla\boldsymbol{u} + \nabla^T\boldsymbol{u}\right)\cdot\boldsymbol{n} = 0,$$

so that the mass conservation is automatically adjusted by the numerical solver. This is a mathematically correct procedure, where an arbitrary value of pressure is selected in one of the outflows. Also, this requires the assumption on the velocity profiles at the other outlet branches, which is arbitrary too. For the above reasons, we decided to mitigate the impact of the adoption of Murray's law and the traction-free section, by using these surrogate data in a "weak" sense through the 3 element windkessel model (3WK). Our approach is to tune the parameters of the 3WK, which is assumed to represent the outflow conditions for our simulations.

The 3WK model is a well-known lumped parameter description of the downstream circulation, that enforces the following relation at the outflows

$$p_b = R_1 Q(t) + (p_b(0) - R_1 Q_b(0))e^{-\frac{t}{CR_2}} + \frac{e^{-\frac{t}{CR_2}}}{C}\int_0^t Q_b(\tau)e^{-\frac{\tau}{CR_2}}d\tau.$$

Here, R_1 and R_2 represent the viscous resistance of the peripheral district, while C represents the compliance. The challenge of using the 3WK model for the boundary conditions is accurately calibrating these parameters. As opposed to adopting parameters based on the literature, here we propose an approach utilizing the available patient-specific data. To this aim, we recall the impedance of the 3WK model, i.e. the ratio between the Fourier transform of pressure and flow rate in the domain of the frequency ω:

$$Z_b(\omega) = \frac{(R_1 + R_2 + \omega^2 C^2 R_2^2 R_1)}{1 + \omega^2 C_b^2 R_2^2} - j\frac{\omega^2 C_b R_2^2}{1 + \omega^2 C_b^2 R_2^2}$$

where $j = \sqrt{-1}$, with

$$|Z_b(\omega = 0)| = R_1 + R_2, |Z_b(\omega \to \infty)| = R_1,$$

while the angle of the impedance has an absolute minimum in

$$\omega_{min} = \sqrt{\frac{R_1 + R_2}{(C_b R_2)^2 R_1}}.$$

We use these values as landmarks to calibrate the parameters for the patient, according to the following algorithm.

(1) A pressure waveform p_{avg} is selected from the literature to be used for the parameter calibration (see Fig. 3).
(2) For each outflow branch, we compute the associated flow rate Q_b based the Murray's law with $s = 2$ and the hydraulic diameters extracted from the patient images. To maintain mass conservation, the flow in the right common iliac artery is computed as the difference between the inflow and the other flow rates.
(3) The Fourier transform of pressure and flow rate for each branch is computed as $Z_b(\omega)$
(4) The parameters R_1, R_2, C are calibrated to match the landmark values of the impedance outlined above, leading to

$$R_1 = |Z_b(\omega \to \infty)|, R_2 = |Z_b(0)| - R_1, C = \sqrt{\frac{R_1 + R_2}{(\omega_{min}R_2)^2 R_1}}.$$

These parameters are computed and then used in each outflow branch for enforcing the 3WK conditions.

Our approach is affected by non-patient-specific choices—as all the others dealing with defective or missing hemodynamics boundary data—however, we argue that the rationale of combining assumptions used and surrogate models for the calibration of the parameters makes our approach robust so that the clinical indications of our simulations are definitely relevant. An extensive validation of this and other procedures is a subject of forthcoming works.

Post-Processing

Details on the computation of flow properties and post-processing can be found in the Supplementary Materials.

RESULTS

Geometrical Reconstruction and FL Evolution

Initially, in 2006, this patient had a small patent FL starting from descending thoracic aorta and extending to left and right common iliac arteries, as shown in Fig. 1. However, the dissected aorta remodeled over 4 years, with enlarged entry tear (0.55 vs. 1.28 cm in diameter), significant dilation of FL (maximum diameter 5.09 vs. 7.76 cm) as well as changes at the iliac bifurcation. The original two distal tears at the left and right common iliac arteries disappeared over the time period and the FL reconnected back through a single distal tear. During the remodeling, cross sections of major proximal branches increased in general. The distal branches, on the other hand, decreased. Detailed geometric information of each major aortic branch, including cross-section area, perimeter as well as hydraulic diameter, are listed in Table 2.

The evolution field obtained by registration is shown in Fig. 2c. The maximum expansion computed by our registration approach was 2.29 cm, collocated with the spot of the largest diameter of the follow-up

FL. The maximum dilation rate was 0.57 cm and spatially averaged dilation rate was 0.22 cm annually. Dilation rates are intended to be averaged over the 4 year period.

Parameter Identification of the Windkessel Model

The 3WK parameters computed with our procedure are listed in Table 3. These values are consistent with data retrieved from the literature, falling in a range of a similar order of magnitude, as shown in Table 4.[3,11,14,23,33] We did not find figures of the 3WK parameters for the renal and common iliac arteries to compare, which are included our geometric models.

CFD

Velocity and Pressure Fields

Streamlines of the blood flow at systolic peak of both initial and follow-up cases are shown in Fig. 4. In both cases, the flow has a significant speed up at the entry tear (216.3 cm/s vs 146.4 cm/s). Significant re-circulation of blood flow was observed inside both FLs, as shown in Fig. 5. The flow in the follow-up cases after remodeling is slower and more helical than that in the initial case in general, as shown in Table 5 and Fig. 5, respectively. The portion of the blood flows into the FL in the initial case is higher (58.2 vs. 53.6%). The pressure of the TL in 2006 is relatively higher than that of the FL at the location distal to the entry tear. After 4 years, the pressure in the FL is higher than that of TL. This corresponds to the reduced blood flowing into the FL.

TAWSS, OSI, RRT

The TAWSS contours are shown in Fig. 6. The FL of the initial case has higher maximum (17.1 vs. 9.7 dyn/cm^2) and spatially averaged TAWSS (2.2 vs. 0.75 dyn/cm^2) than the follow-up case does. The

TABLE 2. Geometrical changes between the initial and the follow-up dissected aortas.

| Location	Perimeter (2006, 2010)	Cross-section area (2006, 2010)	Hydraulic diameter (2006, 2010)
Ascending aorta	(8.35, 9.29)	(5.48, 6.63)	(2.63, 2.86)
Descending thoracic	(7.43, 7.73)	(4.36, 4.70)	(2.34, 2.43)
Brachiocephalic	(2.80, 2.96)	(0.60, 0.69)	(0.86, 0.93)
Left common carotid	(1.88, 1.94)	(0.41, 0.29)	(0.58, 0.59)
Left subclavian	(2.30, 2.14)	(0.41, 0.36)	(0.72, 0.67)
Superior mesenteric artery	(2.04, 2.29)	(0.32, 0.41)	(0.63, 0.72)
Left renal	(1.41, 1.41)	(0.15, 0.15)	(0.44, 0.42)
Right renal	(1.45, 1.10)	(0.16, 0.09)	(0.44, 0.32)
Left common iliac	(2.45/1.88, 2.00)	(0.47/0.28, 0.31)	(0.77/0.59, 0.63)
Right common iliac	(2.67/2.18, 2.46)	(0.56/0.37, 0.48)	(0.83/0.69, 0.77)

Length in cm. Notice that the division TL/FL in the iliac arteries is present only in 2006.

TABLE 3.   Patient specific windkessel parameters of the *initial* and *follow-up* cases.

Artery	R_1 (10^3 dyn·s/cm^2) (2006, 2010)	R_2 (10^3 dyn·s/cm^2) (2006, 2010)	C (10^{-4} cm^5/dyn) (2006, 2010)
Brachiocephalic	(1.22, 0.81)	(7.67, 5.11)	(2.86, 4.21)
Left common carotid	(2.73, 2.02)	(1.72, 1.28)	(1.25, 1.68)
Left subclavian	(1.77, 1.58)	(1.12, 0.99)	(1.92, 2.16)
Superior mesenteric artery	(2.26, 1.36)	(1.42, 0.86)	(1.51, 2.51)
Left renal	(4.73, 3.90)	(2.98, 2.46)	(0.72, 0.50)
Right renal	(4.74, 6.87)	(2.99, 4.33)	(0.72, 0.87)
Left common iliac	(1.53/2.60, 1.79)	(0.96/1.13, 1.13)	(2.23/1.31, 1.90)
Right common iliac	(1.31/1.97, 1.18)	(0.83/1.24, 0.75)	(2.60/1.73, 2.89)

TABLE 4.   Previously published 3WK parameters of arteries.

Artery	R_1 (10^3 dyn·s/cm^2)	R_2 (10^3 dyn·s/cm^2)	C (10^{-4} cm^5/dyn)
Brachiocephalic[3,14,23]	0.13, 0.5, 0.63	3.06, 0.85, 1.71	3.5, 0.95, 1.01
Left common carotid[3,11,14,23,33]	1.18, 0.15, 1.9, 1.76, 2.6	1.84, 1.95, 3.22, 4.17, 2.34	0.77, 0.64, 0.25, 0.41, 1.02
Left subclavian[3,11,14,23,33]	0.97, 0.20, 0.75, 2.41, 1.75	1.52, 1.52, 1.25, 5.47, 2.94	0.92, 0.83, 0.64, 0.31, 0.67
Left ext. iliac[33]	0.85	1.42	0.29
Right ext. iliac[33]	0.84	1.42	0.28
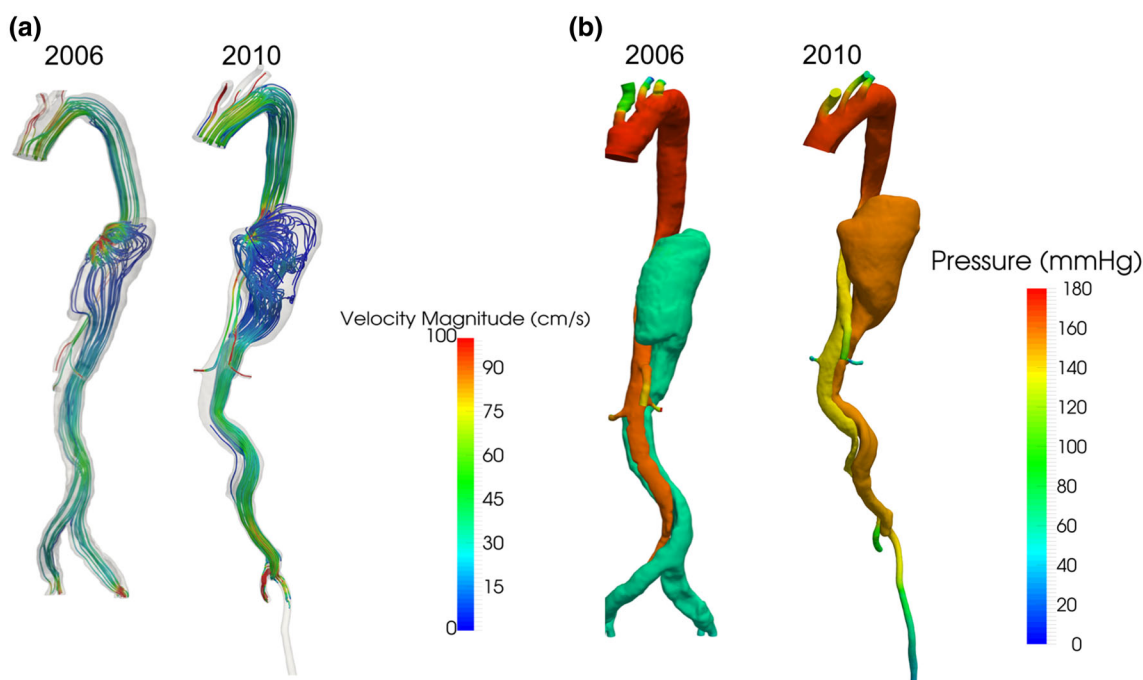
FIGURE 4.   (a) Streamlines collored by velocity magnitude. (b) Pressure contours.

maximum TAWSS of the whole aorta located at the entry tear for both cases (130.4 vs. 43.3 dyn/cm^2), as shown in Fig. 6.

OSI contour plots are shown in Fig. 5b. The surface with highly oscillatory WSS was in the distal of the FL in the initial case. It shifted to the proximal with further aneurysmal dilation. The averaged OSI on FL is higher in the follow-up case (0.12 vs. 0.19).

RRT around the FL surface is shown in Fig. 6c. High RRT indicates more residence time of blood particles near the wall. Relatively low RRT was observed on majority of the wall of FL in both initial and follow-up cases. However, there was a small region with high RRT (over 100 cm^2/dyn) on the distal part of the initial FL and it was shifted to the proximal part of the follow-up case.
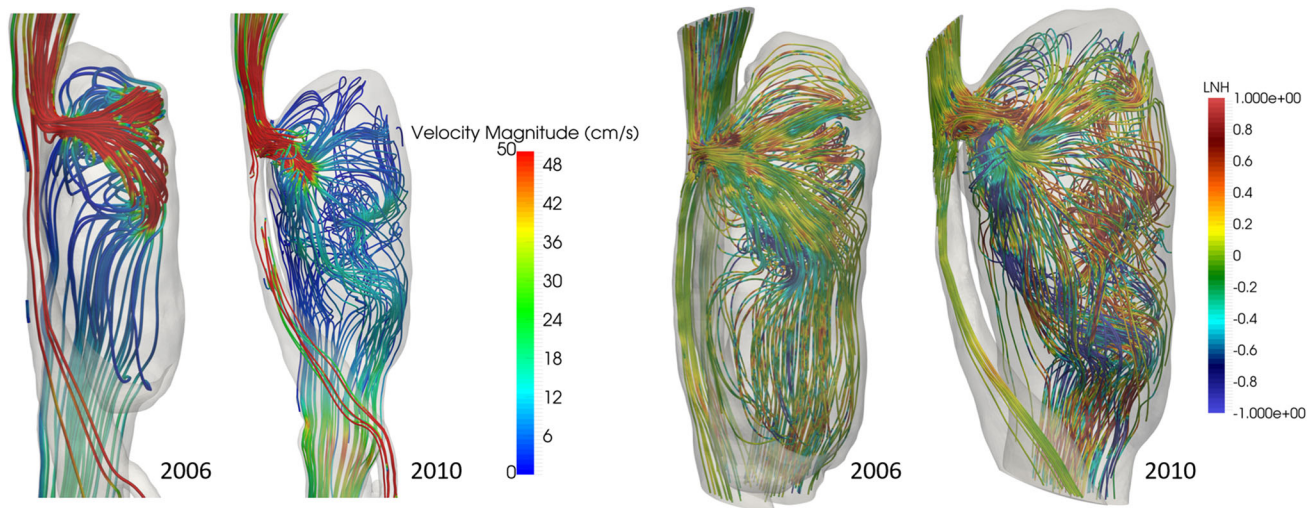
FIGURE 5. Streamlines colored by velocity magnitude (left) and LNH (right) on FLs.

TABLE 5. Hemodynamic properties of the initial and follow-up cases.

Hemodynamics	Artery	Initial (2006)	Follow-up (2010)
Max peak velocity (cm/s)	Ascending	104.7	79.5
	Arch	73.6	49.5
	Proximal to entry	179.7	134.0
	Distal to entry	114.3	112.9
	Entry tear	216.3	146.4
Flow splitting (%)	TL	41.8	46.4
	FL	58.2	53.6
WSS at peak systolic (dyn/cm^2)	Max on FL	22.8	14.6
	Average on FL	3.2	0.61
	Entry tear	155.7	150.8
TAWSS (dyn/cm^2)	Max on FL	17.1	9.7
	Average on FL	2.2	0.75
	Entry tear	130.4	43.3
TAWSS gradient (dyn/cm^3)	Max on FL	266.8	97.9
	Average on F	3.6	1.7
	Entry tear	251.6	240.1
OSI	Max on FL	0.5	0.5
	Average on FL	0.12	0.19

Correlation Between FL Evolution and Hemodynamics

As illustrated in Fig. 7, TAWSS positively correlates with FL evolution. However, the positive correlation is true only for low TAWSS. Figure 7 displays, for each point on the 2006 FL surface (represented by a blue circle), the associated TAWSS (*x*-axis) and the normal deformation. For TAWSS > 2.5 dyn/cm^2, the deformation over the years is constant with the TAWSS. Below this threshold, the correlation is positive (Fig. 7 right). A mild negative correlation was found between OSI and deformation ($r^2 = 0.29$) (See the figure in the Supplementary Materials). The pattern of the RRT is more complex. Figure 8 shows the RRT on the 2006 FL categorized into two classes (RRT ≥ 20 cm^2/dyn). Clearly, the high RRT is only in

the distal bottom of the FL. Figure 8 right shows the normal deformation δ on the 2006 FL. We split four groups: $\delta \leq -0.5$, $-0.5 \leq \delta \leq 0$, $0 \leq \delta \leq 1.5$ and $\delta > 1.5$ (in cm). It is evident that there are two regions with negative deformations over the years. One region is in the distal bottom part of the FL, and features the largest negative deformation. The other region is around the entry tear. The RRT is clearly correlated to the former shrinking region.

DISCUSSION

The study is based on a longitudinal data set of one patient with originally uTBAD, but late FL degeneration. On a basis of the rigorous quantification of the
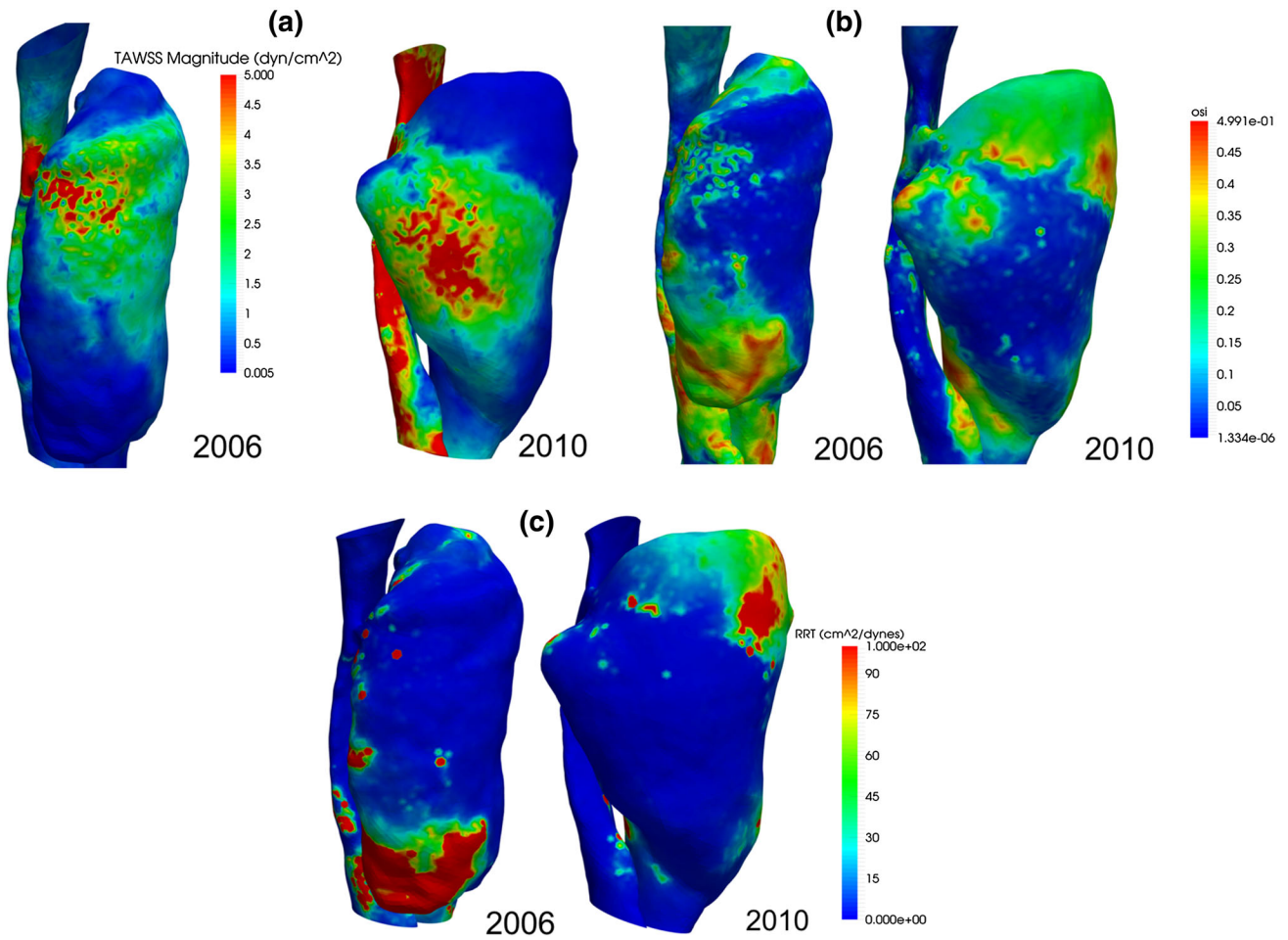
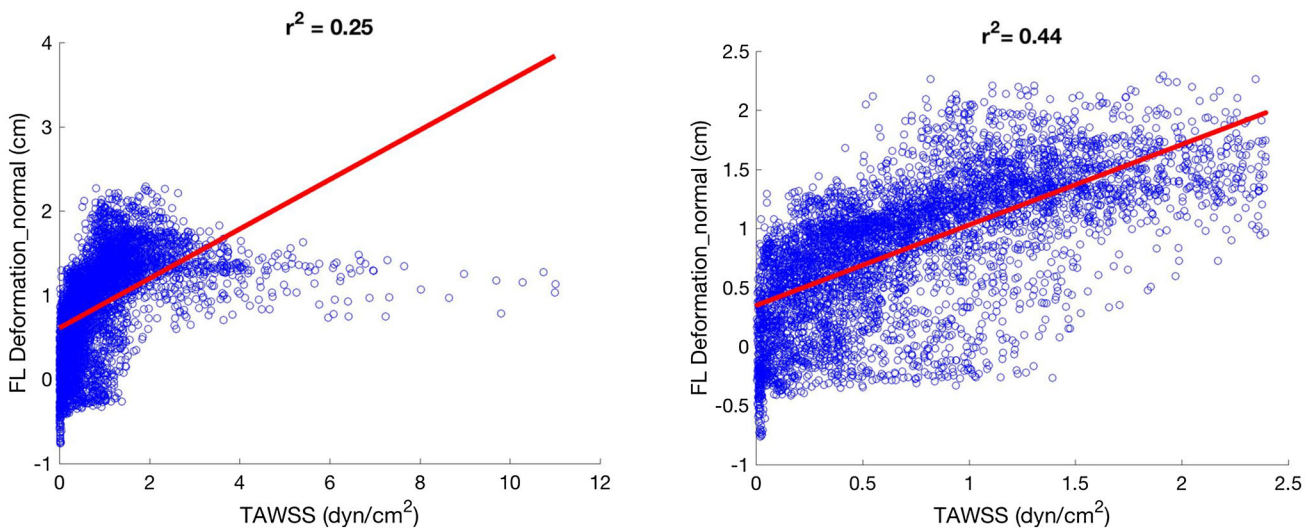FIGURE 6.   TAWSS, OSI and RRT contours on FLs.

FIGURE 7.   TAWSS positively correlates with FL evolution for TAWSS < 2.5 dyn/cm². Each blue circle indicates each point on the 2006 FL surface. Left: Correlation between TAWSS and FL deformation. Right: correlation between TAWSS and FL deformation with TAWSS < 2.5 dyn/cm².
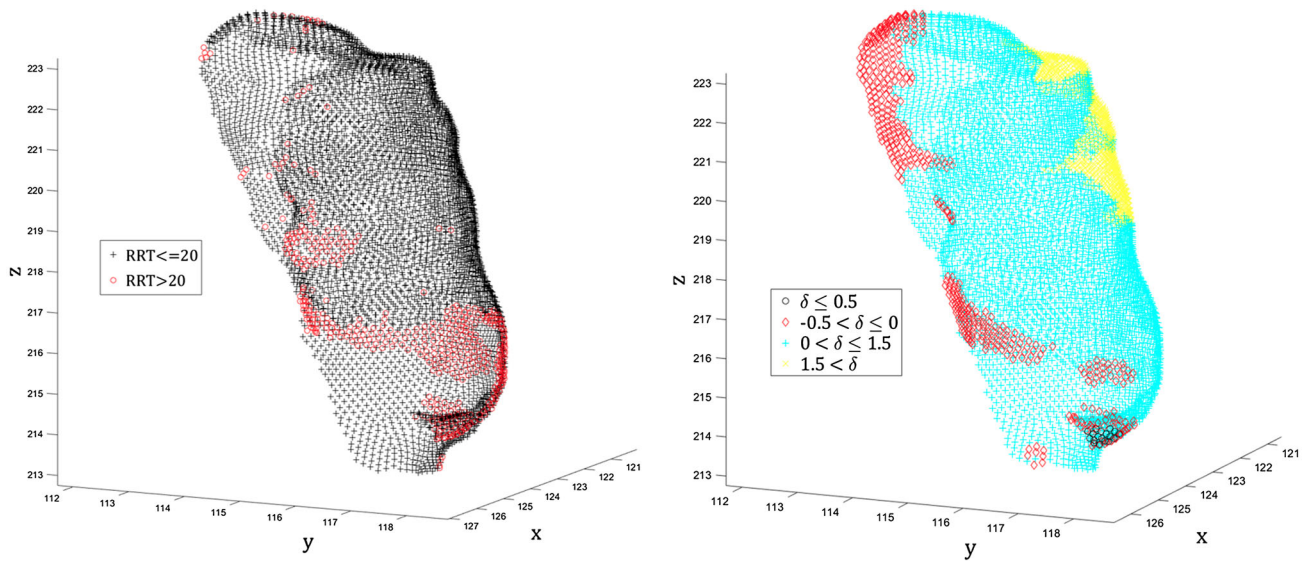
FIGURE 8. Left: Stratification of the RRT on the 2006 FL (blue: RRT $\leq$ 20 cm^2/dyn; red: RRT > 20 cm^2/dyn). Right: Stratification of the normal deformation in 4 groups (unit: cm): $\delta \leq -0.5$, $-0.5 \leq \delta \leq 0$, $0 \leq \delta \leq 1.5$ and δ>1.5. It is evident that there are two regions with negative deformations over the years. One region is the distal bottom part of the FL, which features the largest negative deformation. The other region is around the entry tear. The RRT is clearly correlated to the former shrinking region.

FL progression over the years, we detect possible correlations between the FL progression and several hemodynamics factors computed on the early-stage geometry. High TAWSS, low OSI, and RRT appear associated with FL evolution in this patient.

A recent longitudinal study[34] used CFD laminar solver to identify predictive hemodynamic factors. The FL evolution was quantified by diameter and FL volume solely. The boundary conditions were prescribed by combining measures and literature data. As in our study, high RRT was indicated to be related to negative deformation. Another longitudinal study[5] with no patient-specific boundary data used inflow measurements from volunteers and literature outflow data. The aortic remodeling was quantified only by looking at the maximal diameter and luminal volume. Pressure in the FL was reduced in the follow-up case. A data assimilation study[3] focused on the calibration of 3WK parameters by rigorous minimization difference between the measured pressure and computed pressure from the laminar simulation. Parameters found for 3WK are consistent our results. The overview of the literature above highlights the novelty of our work at the methodological level. As the FL expansion rate has been recognized in the imaging literature as a critical factor, there has been no consensus on quantitative criteria.[9,12,20,27,28] A 3D comprehensive evaluation of the FL deformation combined with the evaluation of patient-specific hemodynamics represents a significant improvement to identify the prognostic factors of the FL aneurysmal dilation. In particular, the added value of our local analysis is to investigate different regional

mechanisms related to different hemodynamic conditions.

The correlation of the TAWSS with the deformation of the FL is apparent only for the region with TAWSS below the threshold of 2.5 dyn/cm^2. For regions affected by larger values of the TAWSS, our study shows no correlation with the remodeling. A similar trend was observed in a previous study,[17] where a direct dose–response relationship was observed between WSS and nitrogen oxides (NO) production in porcine aortic artery. A deeper analysis at the tissue level might facilitate identifying in detail the possible correlations between the two studies.

High RRT has been found to correlate with the thrombosis absorption,[25,34] which is usually considered as a positive event. In our patient, the registration analysis of the FL showed two regions with the negative deformation. One is in the neighborhood of the entry tear. This may be associated with flow re-circulation that may induce fibrotic mechanisms. The other one with the more evident inward remodeling is in the distal bottom part of the FL, where the remodeling seems to be more related to a thrombotic mechanism, with a particle deposition opaque to the follow-up imaging. The correlation with high RRT is apparent only for the second region, consistent with the previous findings.[8,25]

High OSI was found related to intracranial aneurysm rupture in a previous study.[32] However, we found here a mild negative correlation between OSI and deformation. This indicates that OSI may not be the main factor for the FL evolution and other factors may

have more important roles (see more discussion on OSI in the Supplementary Materials).

LIMITATIONS

Our study resorts to state-of-the-art techniques of image processing and computational hemodynamics, yet there are several limitations. The arterial wall is assumed to be rigid, as the computational costs of a systematic fluid–structure interaction simulation are out of reach on a large cohort of patients. In addition, we do not have patient-specific constitutive material model for the aortic wall. Furthermore, the patient-specific pressure and flow data for boundary conditions are missing. A flow rate of a patient from a previous publication with flat velocity profile was assumed due to the lack of patient-specific data. *In vivo* 3D velocity profile measured by PC-MRI has been shown to be more realistic than the flat profile when enforced as inflow boundary condition.[15] The former should be enforced as boundary condition if available in the future follow-up studies. Finally, it is a single patient study, the methodology should be applied to large cohorts of patients in order to draw more substantial clinical conclusions. In the follow-up, we will organize a clinical study in a way that boundary related data could be collected, yet meeting all the constraints of normal clinical practice.

More in general, with the improvement of data collection and computational methods, we will remove many of those limitations. Nevertheless, the combined registration-CFD analysis presented here is a valuable tool to predict which patients with originally uTBAD will develop late complication requiring surgical intervention. In particular, the importance of an accurate local analysis of the geometrical changes over the years is apparent.

CONCLUSIONS

This paper is based on the hypothesis that the aortic geometry plays a major role in the progression of an aortic dissection—corroborated by clinical evidence—and that the hemodynamics is the link. As such, (i) an objective, local quantification of the morphological progression in time is performed, based on image-registration techniques; (ii) systematic CFD analyses are necessary for identifying the prognostic factors in the hemodynamics, showing the role of the fluid dynamics influencing the aortic remodeling and disease progression. The CFD simulation is particularly challenging due to the high computational costs and lack of boundary data. To address these problems,

we propose some novel solutions. Specifically, for the former concern we have proposed an effective LES modeling and for the latter concern, we have proposed an efficient and reliable combination of literature and surrogate models.

Our preliminary results are promising. In particular, TAWSS and RRT were found correlated with the FL evolution. The local analysis of the hemodynamics correlation with the remodeling is informative for different mechanisms. Low TAWSS is associated with deformation only below a threshold that may be correlated to biological dynamics in the arterial wall. The RRT seems to be informative of the possible thrombotic dynamics occurring in the bottom part of the FL. Further validation of these results is needed by applying the approach to a more significant cohort of patients, that could enable us to reach our ultimate goal of developing predictive algorithms based on this methodology.

ELECTRONIC SUPPLEMENTARY MATERIAL

The online version of this article (https://doi.org/10. 1007/s10439-018-2012-z) contains supplementary material, which is available to authorized users.

REFERENCES

[1]Afifi, R. O., H. K. Sandhu, S. S. Leake, V. Kumar, A. Azizzadeh, K. M. Charlton-Ouw, T. C. Nguyen, C. C. Miller, H. J. Safi, and A. L. Estrera. Outcomes of patients with acute type B (DeBakey III) aortic dissection: a 13 year single center experience. *Am. Heart. Assoc.* 2014. https://doi.org/10.1161/CIRCULATIONAHA.115.015302.

[2]Akutsu, K., J. Nejima, K. Kiuchi, K. Sasaki, M. Ochi, K. Tanaka, and T. Takano. Effects of the patent false lumen on the long-term outcome of type B acute aortic dissection. *Eur. J. Cardio-Thor. Surg.* 26:359–366, 2004.

[3]Alimohammadi, M., O. Agu, S. Balabani, and V. Díaz-Zuccarini. Development of a patient-specific simulation tool to analyse aortic dissections: assessment of mixed patient-specific flow and pressure boundary conditions. *Med. Eng. Phys.* 36:275–284, 2014.

[4]Bertagna, L., A. Quaini, and A. Veneziani. Deconvolution-based nonlinear filtering for incompressible flows at moderately large Reynolds numbers. *Int. J. Numer. Methods Fluids* 81:463–488, 2016.

[5] Chen, D., M. Müller-Eschner, D. Kotelis, D. Böckler, Y. Ventikos, and H. von Tengg-Kobligk. A longitudinal study of type-B aortic dissection and endovascular repair scenarios: computational analyses. *Med. Eng. Phys.* 35:1321–1330, 2013.

[6] Cheng, Z., C. Riga, J. Chan, M. Hamady, N. B. Wood, N. J. Cheshire, Y. Xu, and R. G. Gibbs. Initial findings and potential applicability of computational simulation of the aorta in acute type B dissection. *J. Vasc. Surg.* 57:35S–43S, 2013.

[7] Cheng, Z., F. Tan, C. Riga, C. Bicknell, M. Hamady, R. Gibbs, N. Wood, and X. Xu. Analysis of flow patterns in a patient-specific aortic dissection model. *J. Biomech. Eng.* 132:051007, 2010.

[8] Cheng, Z., N. B. Wood, R. G. Gibbs, and X. Y. Xu. Geometric and flow features of type B aortic dissection: initial findings and comparison of medically treated and stented cases. *Ann. Biomed. Eng.* 43:177–189, 2015.

[9] Evangelista, A., V. Galuppo, D. Gruosso, H. Cuéllar, G. Teixidó, and J. Rodríguez-Palomares. Role of entry tear size in type B aortic dissection. *Ann. Cardiothorac. Surg.* 3:403, 2014.

[10] Hebballi, R., and J. Swanevelder. Diagnosis and management of aortic dissection. *Contin. Educ. Anaesth. Crit. Care Pain* 9:14–18, 2009.

[11] Kim, H. J., I. E. Vignon-Clementel, C. A. Figueroa, J. F. LaDisa, K. E. Jansen, J. A. Feinstein, and C. A. Taylor. On coupling a lumped parameter heart model and a three-dimensional finite element aorta model. *Ann. Biomed. Eng.* 37:2153–2169, 2009.

[12] Lobato, A., and P. Puech-Leao. Predictive factors for rupture of thoracoabdominal aortic aneurysm. *J. Vasc. Surg.* 27:446–453, 1998.

[13] Modersitzki, J. Numerical Methods for Image Registration. Oxford: Oxford University Press, 2004.

[14] Moireau, P., N. Xiao, M. Astorino, C. A. Figueroa, D. Chapelle, C. Taylor, and J.-F. Gerbeau. External tissue support and fluid–structure simulation in blood flows. *Biomech. Model. Mechanobiol.* 11:1–18, 2012.

[15] Morbiducci, U., R. Ponzini, D. Gallo, C. Bignardi, and G. Rizzo. Inflow boundary conditions for image-based computational hemodynamics: impact of idealized versus measured velocity profiles in the human aorta. *J. Biomech.* 46:102–109, 2013.

[16] Myronenko, A., and X. Song. Point set registration: coherent point drift. *IEEE Trans. Pattern Anal. Mach. Intell.* 32:2262–2275, 2010.

[17] Nerem, R. M., D. G. Harrison, R. W. Taylor, and W. R. Alexander. Hemodynamics and vascular endothelial biology. *J. Cardiovasc. Pharmacol.* 21:S6–S10, 1993.

[18] Nienaber, C. A., and R. E. Clough. Management of acute aortic dissection. *Lancet* 385:800–811, 2015.

[19] Nienaber, C. A., S. Kische, H. Rousseau, H. Eggebrecht, T. C. Rehders, G. Kundt, A. Glass, D. Scheinert, M. Czerny, and T. Kleinfeldt. Endovascular repair of type B aortic dissection. *Circulation* 6:407–416, 2013.

[20] Onitsuka, S., H. Akashi, K. Tayama, T. Okazaki, K. Ishihara, S. Hiromatsu, and S. Aoyagi. Long-term outcome and prognostic predictors of medically treated acute type B aortic dissections. *Ann. Thorac. Surg.* 78:1268–1273, 2004.

[21] Pape, L. A., M. Awais, E. M. Woznicki, T. Suzuki, S. Trimarchi, A. Evangelista, T. Myrmel, M. Larsen, K. M. Harris, and K. Greason. Presentation, diagnosis, and outcomes of acute aortic dissection: 17 year trends from the International Registry of Acute Aortic Dissection. *J. Am. Coll. Cardiol.* 66:350–358, 2015.

[22] Passerini, T., A. Quaini, U. Villa, A. Veneziani, and S. Canic. Validation of an open source framework for the simulation of blood flow in rigid and deformable vessels. *Int. J. Num. Methods Biomed. Eng.* 29:1192–1213, 2013.

[23] Pirola, S., Z. Cheng, O. Jarral, D. O'Regan, J. Pepper, T. Athanasiou, and X. Xu. On the choice of outlet boundary conditions for patient-specific analysis of aortic flow using computational fluid dynamics. *J. Biomech.* 60:15–21, 2017.

[24] Quarteroni, A., A. Veneziani, and C. Vergara. Geometric multiscale modeling of the cardiovascular system, between theory and practice. *Comput. Methods Appl. Mech. Eng.* 302:193–252, 2016.

[25] Rayz, V., L. Boussel, L. Ge, J. Leach, A. Martin, C. Lawton, C. McCulloch, and D. Saloner. Flow residence time and regions of intraluminal thrombus deposition in intracranial aneurysms. *Ann. Biomed Eng.* 38:3058–3069, 2010.

[26] Shang, E. K., D. P. Nathan, R. M. Fairman, J. E. Bavaria, R. C. Gorman, J. H. Gorman, and B. M. Jackson. Use of computational fluid dynamics studies in predicting aneurysmal degeneration of acute type B aortic dissections. *J. Vasc. Surg.* 62:279–284, 2015.

[27] Song, J.-M., S.-D. Kim, J.-H. Kim, M.-J. Kim, D.-H. Kang, J. B. Seo, T.-H. Lim, J. W. Lee, M.-G. Song, and J.-K. Song. Long-term predictors of descending aorta aneurysmal change in patients with aortic dissection. *J. Am. Coll. Cardiol.* 50:799–804, 2007.

[28] Sueyoshi, E., I. Sakamoto, K. Hayashi, T. Yamaguchi, and T. Imada. Growth rate of aortic diameter in patients with type B aortic dissection during the chronic phase. *Circulation* 110:II-256–II-261, 2004.

[29] Svensson, L. G., N. T. Kouchoukos, D. C. Miller, J. E. Bavaria, J. S. Coselli, M. A. Curi, H. Eggebrecht, J. A. Elefteriades, R. Erbel, and T. G. Gleason. Expert consensus document on the treatment of descending thoracic aortic disease using endovascular stent-grafts. *Ann. Thorac. Surg.* 85:S1–S41, 2008.

[30] Tsai, T. T., A. Evangelista, C. A. Nienaber, T. Myrmel, G. Meinhardt, J. V. Cooper, D. E. Smith, T. Suzuki, R. Fattori, and A. Llovet. Partial thrombosis of the false lumen in patients with acute type B aortic dissection. *N Engl. J. Med.* 357:349–359, 2007.

[31] Tse, K. M., P. Chiu, H. P. Lee, and P. Ho. Investigation of hemodynamics in the development of dissecting aneurysm within patient-specific dissecting aneurismal aortas using computational fluid dynamics (CFD) simulations. *J. Biomech.* 44:827–836, 2011.

[32] Xiang, J., S. K. Natarajan, M. Tremmel, D. Ma, J. Mocco, L. N. Hopkins, A. H. Siddiqui, E. I. Levy, and H. Meng. Hemodynamic–morphologic discriminants for intracranial aneurysm rupture. *Stroke* 42:144–152, 2011.

[33] Xiao, N., J. D. Humphrey, and C. A. Figueroa. Multi-scale computational model of three-dimensional hemodynamics within a deformable full-body arterial network. *J. Comput. Phys.* 244:22–40, 2013.

[34] Xu, H., Z. Li, H. Dong, Y. Zhang, J. Wei, P. N. Watton, W. Guo, D. Chen, and J. Xiong. Hemodynamic parameters that may predict false-lumen growth in type-B aortic dissection after endovascular repair: a preliminary study on long-term multiple follow-ups. *Med. Eng. Phys.* 50:12–21, 2017.

[35] Zamir, M., P. Sinclair, and T. H. Wonnacott. Relation between diameter and flow in major branches of the arch of the aorta. *J. Biomech.* 25:1303–1310, 1992.